A&A 462, 1147–1155 (2007)
DOI: 10.1051/0004-6361:20054700

Astronomy & Astrophysics

Supersonic downflows in the vicinity of a growing pore

Evidence of unresolved magnetic fine structure at chromospheric heights

A. Lagg, J. Woch, S. K. Solanki, and N. Krupp

Max-Planck-Institut für Sonnensystemforschung, Max-Planck-Straße 2, Katlenburg-Lindau, Germany
e-mail: lagg@mps.mpg.de

Received 16 December 2005 / Accepted 26 October 2006

ABSTRACT

Aims. The velocity and magnetic fine structure of the chromosphere at the leg of an emerging magnetic loop is investigated at a location of supersonic downflows.
Methods. We analyze a time series of spectropolarimetric data in the He I 1083 nm triplet covering a time interval of ≈70 min. The temporal evolution as well as the topology of the magnetic field in the downflow region are investigated. We apply an inversion technique based on a genetic algorithm using the Milne-Eddington approach. The technique is very reliable and robust in retrieving maps of the velocity and the magnetic field vector for both atmospheric components separately.
Results. We observe redshifts corresponding to a downflow speed of up to 40 km s^{-1} in the vicinity of a growing pore. These supersonic downflows always coexist with a second atmospheric component almost at rest (slow component) within the same resolution element. The redshifted component is more inclined to the solar normal than the slow component and has a different field strength.
Conclusions. We interpret this downflow as a consequence of the draining of the rising loops. The different magnetic field orientation of the redshifted and the slow component give rise to two possible interpretations: an uncombed structure of the chromosphere, similar to the differently inclined flux-tubes in the penumbra of a sunspot, or a cloud-like structure containing gas at different velocities in two separate height layers of the solar atmosphere.

Key words. Sun: chromosphere – Sun: magnetic fields – Sun: infrared

1. Introduction

Whereas at photospheric layers the well known Evershed flow (Evershed 1909, 1910) is responsible for transporting mass nearly horizontally outward from the umbra, a reversed flow is observed at chromospheric layers. Gas flows along curved magnetic loops are thought to be responsible for this so called reversed Evershed effect (e.g. Maltby 1975; Solanki 2003). Such steady, high speed downflows in the transition region lasting over several hours or even days have been reported in a number of observations (e.g. Gebbie et al. 1981; Dere 1982; Kjeldseth-Moe et al. 1988). These downflows are considered to play a major role in the understanding of the physics of the lower corona: they are manifested in unidirectional flows through active region loops like siphon flows (e.g. Degenhardt 1989; McClymont 1989; Mariska 1988), fallout of spicular material (Pneuman & Kopp 1978), results of nano-flares or explosive events, or the result of chromospheric evaporation and condensation at the loop apex (Müller et al. 2004). However, most of these downflow phenomena have been reported for coronal or transition region lines like C IV (154.8 nm) or O IV (78.9 nm). SUMER observations show that the highest downflow speeds in quiet Sun areas are reached at temperatures between $\log T \approx 5$–5.6 and usually vanish at chromospheric temperatures (Teriaca et al. 1999; Brekke et al. 1997; Peter & Judge 1999). In active regions the velocities peak at lower temperatures ($\log T \approx 4.5$–5).

Strong downflows are also present at much lower temperatures, mainly located in the vicinity of active regions. Kjeldseth-Moe et al. (1988) report a red shift corresponding to a velocity of 67 km s^{-1} for the C II 133.5 nm line, formed at a temperature of ≈26 500 K. Similar to our observation in the He I line (formation temperature 8000–10 000 K), they observe the presence of a second, almost unshifted component within the resolution element of their instrument. These authors find no dependence of the value of the redshift with temperature, only the filling factor of the redshifted component increases with temperature. Brynildsen et al. (2004) finds similar, dual flows in the umbrae and penumbrae of sunspots.

Downflows in the He I 1083.0 nm line were reported by Penn & Kuhn (1995); Muglach et al. (1997); Muglach & Sütterlin (1998). To our knowledge, the first report on dual flows (one subsonic and one supersonic component) in the He I 1083.0 nm line was given by Schmidt et al. (2000). Their analysis of a time sequence shows a steady downflow of up to 42 km s^{-1} lasting several minutes. Strong downflows (up to 40 km s^{-1}) in the He I line were also reported by Teriaca et al. (2003) at the location of a two ribbon flare.

The dual flow structure points to the possibility that these flows occur in an extremely filamentary structure, caused by the magnetic field. To understand these flows the determination of the magnetic field structure in this region is essential. In this paper we analyze data from a region of large redshifts surrounding a site of flux emergence. This region was previously investigated in papers by Solanki et al. (2003) and Wiegelmann et al. (2005). The analysis of a time series of spectropolarimetric data obtained in the He I 1083 nm line allows us not only to retrieve the velocity pattern but also to investigate the magnetic field structure independently for two atmospheric components present in one resolution element: a steady, high speed downflow component

Table 1. Line parameters of the He I triplet.

Line	Wavelength [nm]	Transition	$g_{\rm eff}$	Rel. osc. strength
He (Tr1)	1082.90911	$2s\,^3S_1$–$2p\,^3P_0$	2.0	0.111
He (Tr2)	1083.02501	$2s\,^3S_1$–$2p\,^3P_1$	1.75	0.333
He (Tr3)	1083.03397	$2s\,^3S_1$–$2p\,^3P_2$	1.25	0.556

and a component almost at rest, which we will refer to as the slow component.

In Sect. 2 we describe the data set and briefly introduce the analysis technique. Then in Sect. 3 we describe the properties of the observed downflows regarding their stationary structure and their temporal evolution. In Sect. 4 we discuss the results in the context of previous interpretations for chromospheric downflows. We discuss the measured magnetic field topology in the context of two different models: the "uncombed model" and the "cloud model". Finally, we summarize the results.

2. Data and analysis technique

We analyze data from the Tenerife Infrared Polarimeter (TIP, Martínez Pillet et al. 1999) mounted on the Vacuum Tower Telescope at the Teide observatory on Tenerife from an active region in the course of emergence (NOAA 9451), located at 33°W, 22°S ($\mu = \cos\Theta = 0.8$). The spectral resolution of the instrument was 30 mÅ per pixel, the spatial resolution was limited by the seeing to ≈1.5″. The temporal evolution of the active region was covered by repetitive scans over an interval of 73 min from 15:13 to 16:17 UT with a gap between 15:22 and 15:58 UT due to a calibration measurement. The rms noise of typically $1 \times 10^{-3} I_{\rm c}$, where $I_{\rm c}$ is the continuum intensity, was achieved by an exposure time of 5 s. The 7 Å wide spectral window was centered around the blue He I line (this is henceforth referred to as transition Tr1) at 1082.909 nm and contains two photospheric lines of Si I and Ca I, the chromospheric He I multiplet (see Table 1) and a telluric blend at 1083.2 nm. Note that the Landé factor $g_{\rm eff}$ for the third line is not correct in the papers by Lagg et al. (2004) and Rüedi et al. (1995)[1].

The He I triplet is excited partially due to photoionization from EUV radiation and collisional excitation with electrons at temperatures above 20 000 K (Athay 1965; Andretta & Jones 1997). It shows a complex non-LTE line formation but is nearly optically thin. Fortunately, the magnetic and velocity fields can be deduced without non-LTE calculations. We applied an inversion technique including the Unno-Rachkowsky solution to describe the individual Zeeman components of each member of the triplet to the data (Rachkowsky 1967) combined with a simple, empirical implementation of the Hanle effect. The method has been described in detail by Lagg et al. (2004). For this paper we extended this method to include the effect of incomplete Paschen-Back splitting following Socas-Navarro et al. (2005); Sasso et al. (2005, 2006). The inversion allows the retrieval of the full magnetic vector in the upper chromosphere where the He I triplet is formed.

Additionally, we obtain line-of-sight-velocity maps for the observed regions (see Fig. 1 for the chromospheric velocity map and Fig. 2 for the photospheric velocities). We performed a relative velocity calibration by setting the line shift of the I profile of the Si I line averaged over a region of low magnetic activity ("quiet region") in the scanned region to zero. The telluric H_2O blend at 1083.2109 nm was used as the second reference wavelength. In a second step we compared this relative velocity calibration to an absolute calibration by using flat field data recorded at disk center, again using the Si I line and the telluric H_2O blend as the reference points. This absolute calibration, used for the analysis in this paper, differs by ≈0.5 km s^{-1} from the relative calibration[2]. A part of this difference is likely due to the convective blueshift of the Si I line in the quiet Sun (Nadeau & Maillard 1988). We estimate the error in our velocity calibration to be less than 1 km s^{-1}.

The inversion technique employs the genetic algorithm Pikaia (Charbonneau 1995), which is very robust in finding the global minimum in the parameter space. This technique is capable of retrieving information on atmospheric parameters even when the signals are quite weak or when two atmospheric components are present in the same resolution element and the resulting line profiles partially overlap in wavelength. The information on magnetic field strength and direction for two independent atmospheric components poses a challenge for the minimization algorithm, but is crucial for the present investigation, since the strongest downflows seen in the He I triplet are invariably associated with multi-component profiles. The presence of two velocity components is usually clear, if one of them is supersonic (see Figs. 3 and 4, where two velocity components can easily be distinguished in Stokes I). However, it is less trivial to determine whether the two velocity components are associated with different magnetic vectors. We therefore performed extensive tests in order to clarify the need for two components with different magnetic field strengths and/or orientations. As a criterion for the quality of the fit to the observed Stokes vector we use the "fitness" value of the Pikaia algorithm. This value is maximized by Pikaia in order to find a set of atmospheric parameters which reproduce the observed Stokes vector best. The fitness f is defined as the reciprocal of the sum of the square of the differences between the observed and the fitted Stokes profiles P ($P = I$, Q, U or V), multiplied by the weighting functions $w_{I,Q,U,V}(\lambda)$ (see Fig. 4) and divided by the strength s of the observed profiles ($s_I = \sum_\lambda |I(\lambda) - 1|$ and $s_{Q,U,V} = \sum_\lambda |(Q,U,V)(\lambda)|$):

$$f_P = \sum_\lambda \frac{w_P(\lambda)}{s_P} \left[P_{\rm fit}(\lambda) - P_{\rm obs}(\lambda)\right]^2 \quad (1)$$

$$f = f_I + f_Q + f_U + f_V. \quad (2)$$

For the regions where the velocity separation between the two components is small or where no second component is visible in the Stokes profiles, the dominant component (i.e. the component with the larger filling factor) agreed well to the results of an inversion involving only one magnetic component. All Stokes parameters were normalized to the continuum level prior to the analysis.

We assume that the magnetic field at the height of formation of the He I line completely fills the resolution element. To verify this assumption we performed two component inversions involving one magnetic and one straylight component. We found

[1] The error in the effective Landé factor of the third line was discovered by Socas-Navarro et al. (2004).

[2] A relative velocity calibration was used in the work by Solanki et al. (2003). Improved convergence of the fitting algorithm and the extension of the analysis technique to include the incomplete Paschen-Back splitting additionally lead to small differences between the velocity maps by Lagg et al. (2004) and in this work. Including all these effects results in a difference of ≈0.4 km s^{-1} in the velocities presented in this work and in previously published papers.

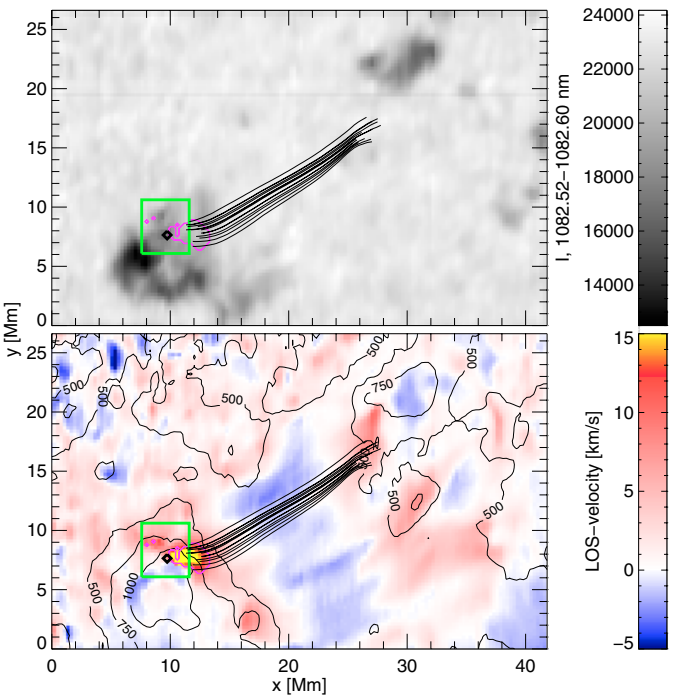

Fig. 1. Continuum (*top*) and line-of-sight velocity map (*bottom*) of NOAA 9451. The velocity map was obtained by a two component inversion, only the component with the larger filling factor is shown. The black contour lines give the values for the magnetic field strength in Gauss as derived from the inversion of the He I profiles. The green box marks "region 1" which is used for further analysis, the black diamond the location of the profile plotted in Fig. 4. The magenta contour line indicates the region where the separation of the two components in wavelength was large enough to allow for the retrieval of two magnetically independent components. To increase the contrast the velocity map saturates at 15 km s^{-1} (the highest velocity values in the yellow region are 40 km s^{-1}). Black lines indicate projections of samples of reconstructed magnetic loops (see Solanki et al. 2003; Wiegelmann et al. 2005).

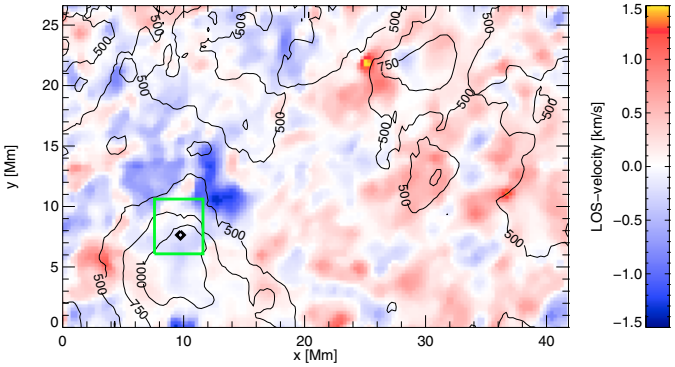

Fig. 2. Photospheric line-of-sight velocity map for the same region as shown in Fig. 1, retrieved from the Si I 1082.7 nm line. The contour lines refer to the chromospheric magnetic field strength as derived from the He I inversions. Note the different velocity scale compared to Fig. 1.

that the straylight component did not improve the quality of the fits to the Stokes vector significantly and that the filling factor of the straylight component is lower than 15% for the relevant regions. Additionally, neglecting the non-magnetic component did increase the stability of the inversion for the magnetic component because of the reduced number of free parameters.

3. Description of observed downflows

3.1. Velocity map

Figure 1 shows the continuum intensity (top panel) and the line-of-sight velocity map (bottom panel) for the observed region as derived from an inversion of the He I Stokes profiles invoking two independent atmospheric components. We show the velocity of the component with the larger filling factor at each individual pixel. The green box indicates the region where we had data to study the temporal evolution of the downflows (see Sect. 3.2). The selection of this region was done during the observations, where we decided to do a fast, repetitive scan over the downflow area already visible in the raw images. The placement of this rectangle is therefore fixed by the observations and does not cover the full area of fast downflows. The orientation of the spectrograph slit is along the y axis, the scan was performed perpendicular to the slit direction along the $+x$ axis.

The blue shifted profiles in the center of the lower half of the image were interpreted as the tops of freshly emerged loops transporting relatively cool material to the upper chromosphere with velocities of up to 4 km s^{-1} (Solanki et al. 2003). We identified these loops by tracing the magnetic field direction obtained from the inversion of the He I Stokes vector (see black lines in Fig. 1). The dominant component, i.e. the component with the larger filling factor, was used for this loop tracing. The reconstructed loops are in good agreement with non-linear force-free field extrapolations (Wiegelmann et al. 2005) from the photospheric field map, which was obtained by applying the inversion code SPINOR (Frutiger 2000; Frutiger et al. 2000) to the Si I line contained in the spectral window of the observations. The legs and footpoints of these loops are associated with red shifted line profiles. The yellow area indicating the fastest downflows is located close to a young pore (see continuum image in Fig. 1) in the direction of the neutral line spanned by the loops.

Figure 2 shows the photospheric velocity map obtained from the inversion of the Si I line. For comparison, we show the same contour lines as in Fig. 1, indicating the magnetic field strength obtained from the He I line. The dominant chromospheric pattern with a central upflow region surrounded by downflowing material is not present in the photosphere. At the position of the fastest chromospheric downflows the photospheric velocities are around 0 km s^{-1}. In the course of the time series (discussed in Sect. 3.2) the photospheric velocities at this position increase to $\approx$0.7 km s^{-1}.

Figure 3 shows the Stokes I profiles at selected positions along a loop from the loop apex (top profile) to the loop footpoint (bottom profile). In the loop apex the blueshift (2–4 km s^{-1}) is clearly visible. With decreasing height of the loop the line center shifts towards the red, reaching values of up to 40 km s^{-1} at the footpoint, where an almost unshifted atmospheric component coexists with the redshifted component. Figure 3 suggests that the redshifted component is the continuation of the loop. The reconstruction of the loops, where we followed the magnetic field direction of the dominant component, i.e. the component with the larger filling factor, confirms this.

In areas of fast downflows (>10 km s^{-1}) a satisfactorily fit to the Stokes vector was only possible under the assumption of a two-component atmosphere, a downflow component showing redshifts of up to 40 km s^{-1} and an almost unshifted component. Figure 4 shows an example of such a profile (see black diamond for the location of this profile in Fig. 1). The observed Stokes vector (black) contains the Si I line at 1082.709 nm, the He I

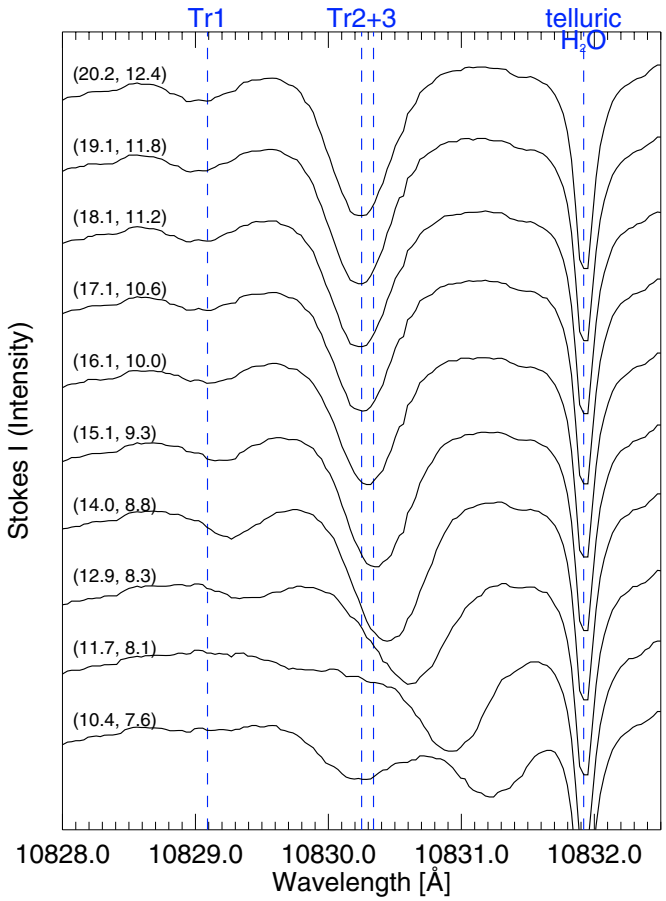

Fig. 3. Stokes I profile along a reconstructed magnetic loop from the loop apex (*top profile*) to the footpoint (*bottom profile*). Close to the footpoints the supersonic downflow component becomes clearly visible. The vertical, dashed lines show the nominal wavelengths of the three components of the He I triplet (transitions Tr1, Tr2 and Tr3). The numbers above each profile indicate the x and y position in Fig. 1 (in Mm).

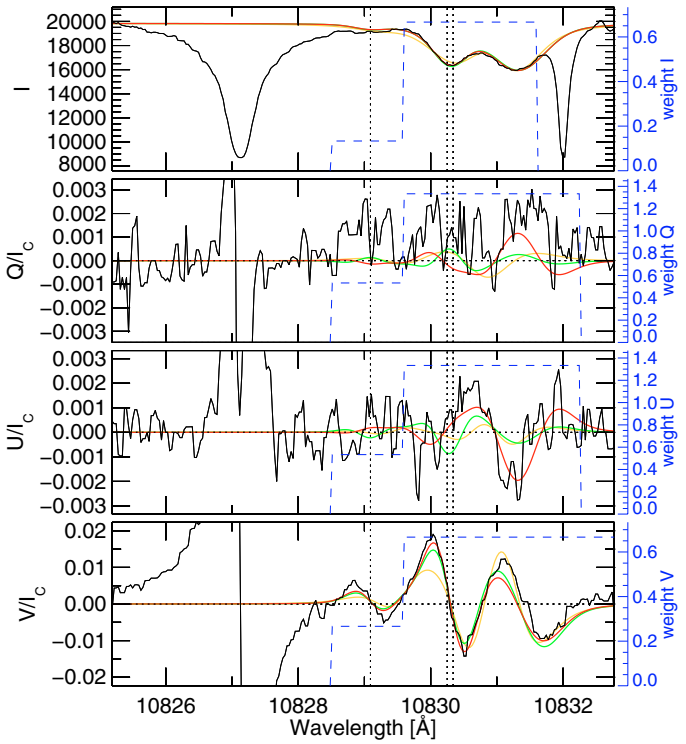

Fig. 4. Stokes profiles showing two distinct magnetic components for the pixel indicated by the black diamond in Fig. 1. The observed profiles are shown in black, the fits in red (two independent magnetic components, $B_{\rm slow}$ = 725 G, $\gamma_{\rm slow}$ = 30° and $B_{\rm fast}$ = 1194 G, $\gamma_{\rm fast}$ = 68°, fitness f = 2.10) and green (2 magnetic components with coupled magnetic field $B_{\rm slow} = B_{\rm fast}$ = 642 G, $\gamma_{\rm slow} = \gamma_{\rm fast}$ = 61° , fitness f = 1.71). The two components are shifted by 28 km s^{-1} relative to each other. The orange line shows a fit assuming one broad absorbing component superposed with a central emission component (fitness f = 1.50). The fit involving two independent magnetic components best reproduces the observed Stokes vector. The dashed, blue line indicates the weighting scheme used for the inversion, the vertical, dotted lines show the central wavelengths of the three components of the He I triplet.

triplet (1082.909 nm, 1083.025 nm and 1083.034 nm, see vertical dotted lines for the position of the central wavelength of these lines), and a telluric H_2O-blend at 1083.2 nm. It is quite obvious, e.g. from the Stokes V profile, that both atmospheric components contain a magnetic field. The red line was obtained by applying a fit with two different atmospheric components, each consisting of the free parameters magnetic field strength (B), its inclination and azimuthal angle (γ and ϕ), the line-of-sight velocity ($v_{\rm LOS}$), the Doppler broadening of the line ($\lambda_{\rm Dopp}$), the gradient of the source function (S_1, enforced to be the same for both components) and one filling factor describing the strength of the two components relative to each other. The weighting scheme used for the χ^2 minimization, indicated by the dashed blue line (the weights were distributed differently over the wavelength for the different Stokes parameters), was chosen to minimize the effects of the telluric blend in Stokes I and to account for the photospheric Ca I blend in the blue He I line. Stability of convergence and reliability of the recovered magnetic field direction was increased by doubling the weight given to Stokes Q and U. The Si I line was fitted separately using SPINOR in order to retrieve the flow velocities in the photosphere (not shown). This line always exhibited a single magnetic component.

In order to reduce the number of fit parameters we tried to fit the He I profiles with a coupled magnetic field vector, i.e. where field strength and direction of both atmospheric components were required to be the same. However, when the separation of the two components is large and the signal in Stokes V is strong the quality of the fit increased significantly when allowing for two uncoupled magnetic components. This clearly indicates that the two components have different magnetic field vectors. The red line in Fig. 4 shows the best fit to the observations using two independent magnetic components, i.e. where magnetic field strength and direction for both components are free parameters. We compare this fit with the best fit to the data assuming that the magnetic field for both atmospheric components is the same (green line). In particular, the observed Q and U profiles are far better reproduced by the red profiles than by the green ones. A reliable determination of the magnetic field vector for both components individually is generally possible if the two components are shifted by at least 10 km s^{-1} and if the filling factors of both components are similar. The magenta contour line in Fig. 1 encloses the pixels where these requirements are fulfilled. For such pixels the use of two independent magnetic components improved the fitness by between 5 and 25%.

We also checked for the possibility of looking at a very broad He I absorption feature superimposed by an emitting component at approximately the same velocity. The orange line in Fig. 4

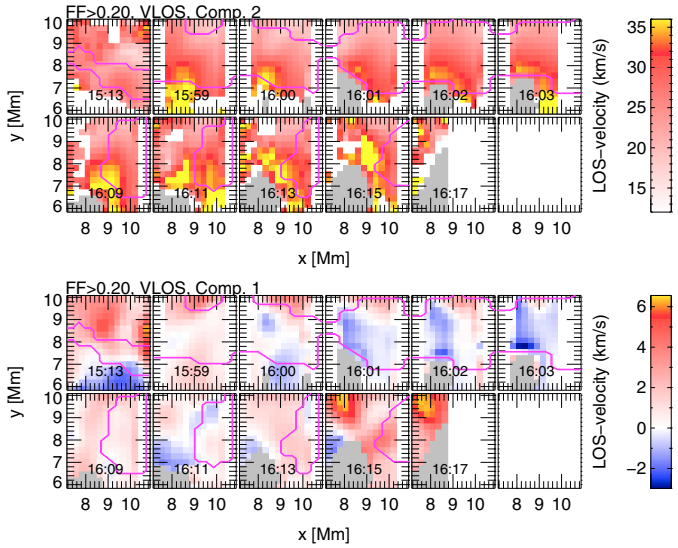

Fig. 5. Temporal variation of LOS-velocity in the region of maximum downflow, for the fast component (*top*) and the slow component (*bottom*). The presented area corresponds to the area within the green rectangle in Fig. 1 ("region 1", size 3×3 Mm^2). The observations span an interval of 73 min. The fast component of a 2-component model is plotted only if the filling factor is larger than 0.20. The area where the He I-line goes into emission is marked in gray. The magenta contour line encloses the region where the separation and filling factor of both components allow for the retrieval of the magnetic field vector separately for both components. Note the difference in velocity scale for the two components.

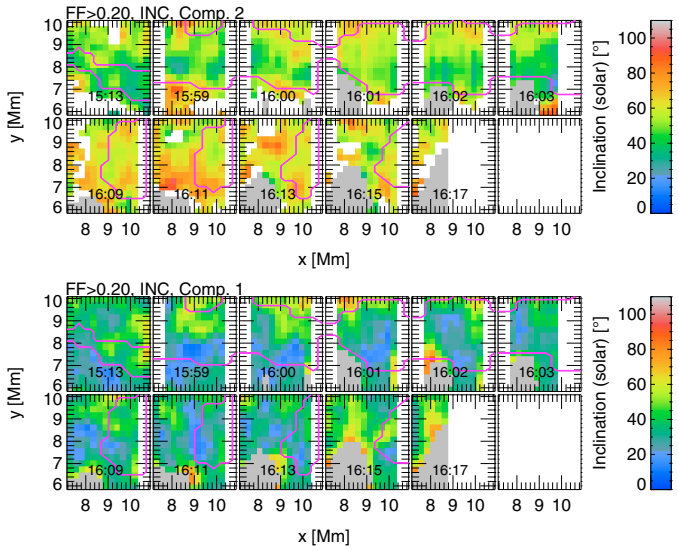

Fig. 6. Same as Fig. 5 but for inclination angle of fast (*top*) and slow component (*bottom*) in the solar reference frame. The same color scale is used for both components.

shows the best fit to the observations under the assumption of an emission profile superimposed onto a broad absorption profile. Even when allowing for two completely independent magnetic components this model does not produce a satisfactory fit to especially Stokes I, Q and U. We therefore conclude that the Stokes signal is produced by two absorbing, magnetic components at different velocities.

Note that in addition to the region of rapid downflow in the bottom left of the scan, a smaller such feature was also found in the top-right part of the frame (Fig. 1). This is also associated with a growing pore, although a smaller one. Here the velocities reach values of up to 15 km s^{-1}, the chromospheric magnetic field strengths are between 700 and 900 G and therefore substantially lower than the field strength in the pore to the lower left (up to 1300 G). Note also that these regions of supersonic downflows are located at opposite footpoints of the same or neighboring loops.

3.2. Temporal evolution

The area of fastest downflow velocities is located near the left footpoint of the largest magnetic loops ("region 1" in Fig. 1). After recording the map presented in Fig. 1 we performed fast, repetitive scans over this region with a time resolution between 1 and 5 min in order to monitor the evolution of the downflows. The time series of velocity maps and magnetic field maps obtained from these scans for the fast and slow chromospheric component retrieved from the He I line are presented in Figs. 5 to 7. The last sub-frame (16:17 UT) is incomplete. The 11 sub-frames were recorded in three sets of measurements: in the first measurement a large scan over the active region was performed (see Fig. 1, UT 15:13), the second and third measurement contained repetitive scans from UT 15:59–16:03 and 16:09–16:17, respectively. The length of the first scan and the calibration measurement carried out after it are responsible for the long time between the first and second sub-frames. The sub-frames of the individual measurements are aligned during the observations by the correlation tracker mounted at the VTT. The spatial alignment of three measurements was achieved by cross-correlating the continuum images.

The fast downflow (>30 km s^{-1}) in the upper chromosphere is evident over the whole time interval of our observations (see Fig. 5). Towards the end of this interval the area of the downflow region as well as the maximum velocities increase. Close to the region where the velocities reach values of more than 35 km s^{-1} the He I line goes into emission (gray areas in Figs. 5–7). The slow component shows a larger relative variability: we observe downflows (<5 km s^{-1}) and upflows (<3 km s^{-1}).

Unlike the fast downflows, which are observed quite frequently, emission features in He I 1083 on the solar disk seem to be a relatively rare phenomenon. In our archive of observations we found only three other datasets with He I emission, two of them also located very close to a pore and one in the vicinity of a two ribbon flare. Unfortunately our data do not allow for a systematic analysis of the emission feature. The simultaneously observed Hα slit jaw images do show an indication for a brightening at the locations of the emissions. Unfortunately, the slit jaw images were overexposed and do not allow for a more detailed analysis of a possible correlation between Hα brightenings or flaring and He I emission.

Our analysis technique is not optimized to produce reliable results for emission profiles, particularly if the true profile may be a mixture of an emission and an absorption profile (filling in). We therefore mark these regions in gray in Figs. 5–7 and exclude these points from further analysis. However, using a two component atmosphere with one absorbing magnetic component and a second, completely independent emitting magnetic component we are able to obtain quite reasonable fits to the observed Stokes I and V profiles (the emitting component is characterized by a negative gradient of the source function). An example for such an emission profile is shown in Fig. 8. The signal in the Q and U profiles is below the noise level (and therefore not shown in Fig. 8), possibly caused by the superposition of the emitting

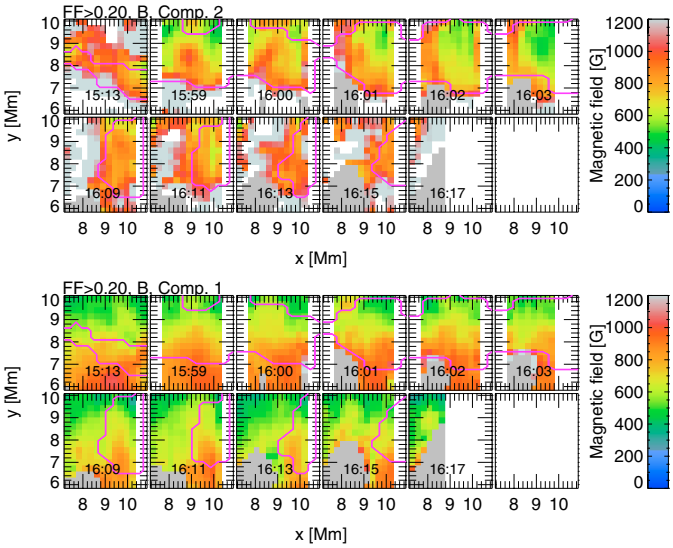

Fig. 7. Same as Fig. 5 but for the magnetic field strength of fast (*top*) and slow component (*bottom*). The same color scale is used for both components.

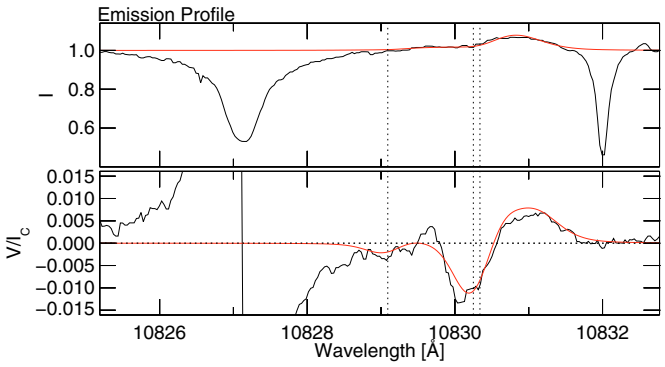

Fig. 8. Typical emission profile (Stokes *I* and *V* only), taken from gray shaded area in Fig. 5. The emission signal is redshifted by ≈10 km s^{-1}. The red line shows the best fit profile assuming one absorbing component and an independent emitting component.

component and the absorbing component. Typically the emission profiles only show one clear velocity component, which is redshifted, but not so strongly as the fast downflows observed in nearby pixels displaying the He I line in absorption. It is interesting to note that the emission profiles seem to be located at positions, where in the preceeding sub-frame high velocities are measured. Also, the increase of the area covered by high velocities leads to spreading of emission profiles at a later time.

We already showed that the two atmospheric components have different magnetic field vectors in the region of large redshifts. In Figs. 6 and 7 we present inclination angle and magnetic field strength for the fast (top) and the slow (bottom) component. To convert the angles from the line-of-sight to the solar reference frame we had to solve the 180° ambiguity problem. From the two possible solutions we selected the one matching the magnetic field extrapolations of Wiegelmann et al. (2005). Since Pikaia looks for the absolute minimum in the χ^2 hypersurface and does not depend on the choice of the initial guesses, the fact that the inclination angle maps shown in Fig. 6 are relatively smooth suggests that this parameter is relatively reliably determined. In the region where a reliable determination of two independent magnetic components is possible (enclosed by the magenta contour lines) the fast component is inclined 40° to 70° to the solar surface (90° inclination means parallel to the solar surface). The slow component usually is between 10° and 40° more vertical than the fast component. The magnetic field strength for the slow component is slightly decreasing with time, whereas the field strength for the fast component undergoes stronger variations and is in general stronger than the field strength of the slow component (see Fig. 7).

The photospheric velocities underlying this region of fast downflow initially is almost at rest (see Fig. 2). During the 73 min interval of observations the photospheric velocities increase by ≈0.7 km s^{-1} (not shown). The velocities of other regions in the scan, including non-magnetic regions, remained almost unchanged. We can exclude *p*-modes as being responsible for this increase in velocity, since our temporal sampling between sub-frames 2 to 6 and sub-frames 7 to 11 would uncover the 5 min periodicity. No significant temporal changes in other parameters, like magnetic field or Doppler broadening, are noticeable in the photosphere.

4. Discussion

The sound speed at the typical formation temperature of the He I line of 8000–10 000 K, is in the order of 10 km s^{-1}. The velocities of up to 40 km s^{-1} measured near one footpoint of the emerging loops clearly exceed the sound speed. This velocity corresponds to a free-fall height of ≈2.5 Mm above the formation height of He I. The free fall velocity from material coming from the loop top (height of ≈10–15 Mm) reaches 70–90 km s^{-1}. The loop height was determined by tracing the magnetic field information retrieved from the He I line (method described in Solanki et al. 2003). The line-of-sight velocity of the downflowing material is significantly below the free fall speed, possibly caused by the deceleration due to underlying plasma. This phenomenon was investigated by Müller et al. (2005) for Hα filtergrams. That the velocities are sub-free-fall is also true when we consider vertical velocities rather than the line-of-sight component. The velocity in the photosphere at the loop footpoint varies from around 0.4 km s^{-1} at the beginning of the observation to 1.1 km s^{-1} downflow at the end of the 70 minute time interval. The photospheric velocity therefore is clearly subsonic, implying the presence of a shock in between the sampled photospheric and chromospheric layers.

4.1. Models for the redshift

Chromospheric redshifts in the range observed in this work have been reported by several authors (see e.g. Kjeldseth-Moe et al. 1988; Penn & Kuhn 1995; Muglach et al. 1997; Muglach & Sütterlin 1998; Balasubramaniam 2001; Spadaro et al. 2004). Some of these authors also found evidence for the coexistance of two flow components in a single spatial pixel. A number of processes have been proposed which produce downflows along field lines. Most attractive in the present context are processes which are related to the emergence of magnetic flux from the photosphere. Properties of emerging flux regions (also called arch filament systems) are summarized in a review by Chou (1993). Downflows in this region can be explained as a result of the pressure balance between the rising flux tube and the surrounding atmosphere. As a consequence of the pressure balance, the flux tube has either to expand or to be emptied, the hydrostatic support of the material above is lost, causing the material in the upper layers of the flux tube to drain to the solar surface. The general observed line-of-sight structure corresponds well to this

picture, with an upflow at the loop top and downflows along the loop's legs.

Using the Echelle spectrograph on the VTT Schmidt et al. (2000) detected redshifts in the range of 40 km s^{-1} in Hβ and the He I 1083 nm line in an active region close to a pore over a period of 90 s. They also reported the presence of an unshifted atmospheric component within the resolution element, very similar to what we see in our observations. They interpreted this signature as a free fall of matter, either unobstructed by magnetic structures or along magnetic field lines, from the height of formation of the He I line (≈2 Mm) down to the photosphere. They assumed the atmospheric layer producing the unshifted absorption to be at higher altitudes, otherwise the falling material would have to cross this layer and alter or even destroy the unshifted line. Our observations show a smooth increase of the redshifts along a loop-like structure (see Fig. 3), starting as a weak blue shift near the loop top and becoming increasingly redshifted towards the footpoints (cf. Fig. 1), indicating that the downflow originates from the loop apex and not at the nominal height of the He I line formation.

Another explanation comes from the convective collapse undergone by photospheric flux tubes after they appear at the solar surface (i.e. the footpoints of loops). The convection is suppressed by the magnetic field (Parker 1978; Spruit 1979; Grossmann-Doerth et al. 1998), causing the material in the flux tube to cool down since the advective heating from hot material underneath the flux tube is stopped. The cold material condenses and drains along the field lines. Although the effect is restricted to convectively unstable layers, such a downflow removes the hydrostatic support for the overlying chromospheric gas, causing it to flow down as well. However, the convective collapse is completed within a few minutes (Grossmann-Doerth et al. 1998), so that the associated downflow is not expected to last for over an hour, as we observe.

Brynildsen et al. (2001a) report on supersonic downflows in sunspot plumes. Almost every unipolar sunspot they analyzed shows a plume, but they also find a high probability for plumes above bipolar regions, like the one described in this paper. In some plumes they observe two flow components (Brynildsen et al. 2001b). The flow speeds reach values of up to 40 km s^{-1} in the corona, peaking at a temperature of $\log T \approx 5.5$. The observed chromospheric velocities in the plumes are between 5 and 10 km s^{-1}, although velocities in the C II line (temperature of formation 26 500 K) reaching values of up to 67 km s^{-1} have been observed (Kjeldseth-Moe et al. 1988). According to Brynildsen et al. (2001a), these velocities are the signature of siphon flows. Siphon flow models of loop flows driven by asymmetric heating are also able to produce strong redshifts in transition region and chromospheric lines (Thomas & Montesinos 1991; Boris & Mariska 1982; McClymont & Craig 1986, 1987; McClymont 1989; Mariska 1988; Spadaro et al. 2003). These models explain a steady redshift at one of the loop legs, either by different field strengths at the two loop foot points (as observed by Rüedi et al. 1992) or by strongly asymmetric heating at the footpoints. These models fail to reproduce the downflows in both loop legs.

We interpret the signature of relatively symmetric downflows in both legs of the magnetic arcade as a mass flow resulting from the upward motion of the freshly emerging flux tubes. These tubes subsequently carry the relatively cool, photospheric material to higher layers at the position of the magnetic neutral line (center of the loops). This upflow can be seen in Fig. 1 (blue region between high downflow velocities). Without subsequent upward transport of material a loop would be emptied by drainage in about 20 min (Chou 1993). This still cool material flows down along the field lines, with higher downflow speeds towards the region with larger field strengths and cooler gas, which is the trailing side of NOAA 9451. This asymmetry is consistent with the observations by Spadaro et al. (2004), who investigated the line-of-sight velocities derived from Hα profiles in an arch filament system during flux emergence. Spadaro et al. (2004) also reported downflows (17 km s^{-1}) on the trailing side of the arch filament system.

From the velocity map in Fig. 1 it is clear that the region of very fast, supersonic downflows is localized at the edge of a young pore, which evolved into a sunspot during the next couple of days. Given the large inclination of the field lines and their direction, the field lines supporting the supersonic flow very likely end in the pore. We propose that rapid chromospheric downflows over forming pores have to do with the cooling of the gas and the probable concentration of the field, which happens in parallel. Both processes lower the gas pressure at a given height, the magnetic concentration by enhancing the Wilson depression, the cooling by decreasing the pressure scale height. These effects can lower the gas pressure in the chromosphere by an order of magnitude compared to the gas pressure in the surrounding plage or quiet Sun (cf. according to the atmospheres of Maltby et al. 1986[3]). Thus the gas draining down from the rising cool loop can fall further until it hits upon stably stratified gas at a given pressure, resulting in higher downflow velocities.

At the location of the supersonic downflows in the chromosphere we observe downflows of a few 100 m/s in the photosphere, retrieved from the Si I line. If the photospheric downflow is driven by the supersonic chromospheric downflows then the mass flux j ($j = \rho v A \alpha$, ρ = density, v = velocity, A = cross sectional area of the downflow and α = filling factor) for the two layers must be conserved. Using the photospheric density as retrieved from the inversion of the Si I line involving one magnetic component and a straylight component (inversion code SPINOR, Frutiger 2000) we can estimate the density at chromospheric heights using a simple, plane parallel atmospheric model. The filling factor in the photosphere is >0.8, in the chromosphere we assume that the magnetic field fills all available space ($\alpha = 1$). The density ratio between the photosphere and the chromosphere turns out to be 10^9, compared to a ratio in velocities of ≈100. This means that the downflow of material in the photosphere can by far not be attributed to the chromospheric downflows, unless the magnetic field lines supporting the downflows spread out by a very large factor. The fact that the downflows in the two layers cover roughly similar areas implies that the increase in photospheric downflows is not just fed by the supersonic chromospheric downflow.

The finding that the downflow speed tends to increase with time at the scanned loop footpoint (Fig. 5) agrees well with the picture of the rising, draining loop. In the hour separating the first and the last images the loop can have risen by 7600 km, assuming a constant rise speed of 2 km s^{-1}. The increased potential energy of the gas at the loop apex may explain the increase in downflows speed with time.

[3] The Photospheric Reference Model of Maltby et al. (1986) gives a density of 1.2^{-9} kg m^{-3} at a height of ≈1700 km (i.e. the assumed formation height of the He I absorption, cf. Avrett et al. 1994). Assuming a Wilson depression of 300 km (Mathew et al. 2004) we compare this density with the Umbral Core Model M at 2000 km, which is 1^{-10} kg m^{-3} (factor 12).

4.2. Models for the emission

As shown in Fig. 8 some profiles show a clear signature of He I emission. The region of emission is close to the region of fastest downflow velocities. The size of the emission region increases with increasing values for the downflow velocities (see gray shaded area in Fig. 5). The He I emission can be interpreted as the signal of a local heating process caused by the transition of the downflowing material from super- to subsonic velocities (Cargill & Priest 1980). This interpretation is consistent with the observed spreading of emission profiles in time, following the increase of the area covered by high velocities. Another possibility is that the emission signal is caused by a small flare at the boundary between the pore and the surrounding plage region. The Hα slit jaw images recorded during the observations do indeed show an indication for brightening in this region, the poor quality of these overexposed images, however, does not allow for a conclusive statement whether an Hα flare occurred or not. A flare was reported from NOAA Space Environment Center (SEC) for this region from 16:07 until 16:14 UT, classified as an SF event, the smallest and faintest kind of flare. However, we were unable to find a dataset to verify whether this flare originated from the area of the observed two-component downflows. Note also that the emission profiles are seen already 6–7 min prior to the flare and are unlikely to be a result of it.

This emission signature presents evidence for an interaction of the downflowing material with a layer at rest. One interpretation of the He I emission line is that the line is driven into emission at the shock formed at the transition of the supersonic downflow to subsonic velocities, which happens between the formation heights of the He I triplet and the Si I line. Alternatively the shock may be located between the heights at which the slow and fast line components of He I are formed (see Sect. 4.3). The fact that with time, as the downflow speed increased, the line went into emission at locations where previously the downflows have been strongest is consistent with the shock rising to higher layers for stronger downflows and eventually becoming visible as an emission in He I. Although the presence of shocks had been deduced earlier (e.g. Degenhardt et al. 1993; Martínez Pillet et al. 1994) this is the strongest direct evidence for shocks.

4.3. Magnetic fine structure of the upper chromosphere

The magnetic field information obtained from both velocity components individually allows us to sketch the magnetic field configuration in the regions of fast downflows. It is evident from Fig. 6 that the fast component is more inclined than the slow component. The size of the area of two different magnetic components is 3×5 Mm^2, considerably larger than our spatial resolution of $\approx$1 Mm (corresponding to 3 pixels in our image). Two possible interpretations to explain this signature are sketched in Fig. 9: if the He I absorption signal is produced in only a single layer located at a specific height above the photosphere, then the chromosphere must consist of differently inclined flux tubes with diameters less than our spatial resolution coexisting next to each other ("uncombed chromosphere"). This situation is shown in Fig. 9a. The more horizontal field lines, carrying the fast downflows, are indicated by the yellow arrows, the red arrows represent the field lines carrying the slow component. We also show the inclination of the photospheric magnetic field as retrieved from the inversion of the Si I line. By carrying out three-component inversions for the photospheric layer (two magnetic components and a straylight component) we tried to connect the differently inclined chromospheric field lines down to the photospheric layer. The three-component inversions did not reproduce the observed photospheric profiles significantly better than the two-component model, consisting of one magnetic component and a straylight component. Also, the retrieved parameters were more unstable with three components (i.e. they varied strongly from one pixel to the next). The Si I line seems not to be sensitive enough to determine the connection between the photospheric and the chromospheric layer.

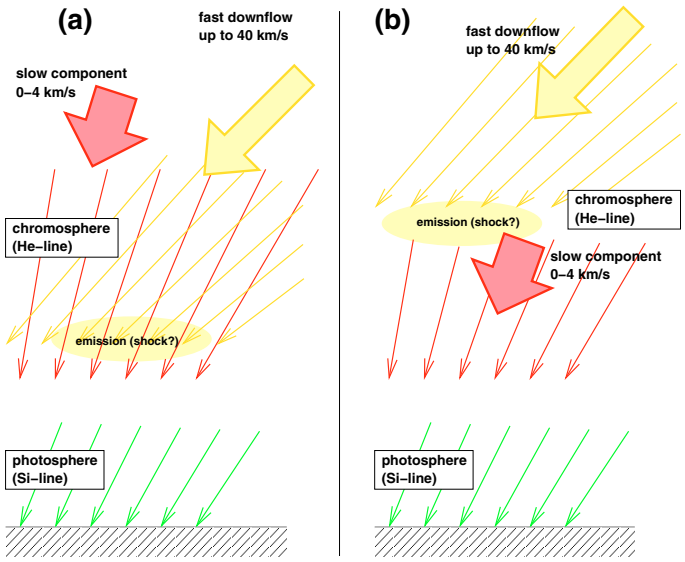

Fig. 9. Sketch of the possible magnetic field topologies at a loop footpoint. **a)** The "uncombed model" is indicated by the different inclination angle between the flux-tube field lines (yellow) and the surrounding field lines (red) in the upper chromosphere. **b)** In the "cloud model" the two different velocity components originate from different heights, the fast downflow component lying above the slow component. The photospheric field obtained from the inversion of the Si I line is indicated by the green arrows. The inclination angles of the arrows represent the measured magnetic field direction. The emission region, possibly caused by a shock, is indicated by the yellow area. Note that the height information is not to scale.

Since the He I absorption signal is optically thin, the observer could also see two clouds of He gas at different altitudes ("cloud model", sketched in Fig. 9b). From the observations alone it is not possible to say whether the fast flowing or the slowly flowing chromospheric gas lies higher. The good match between the extrapolations of the photospheric field vector (see Sect. 3.1) and the magnetic field vector determined from the dominant He I component, which is the fast component close to to the pore, suggests that the cloud containing the fast gas lies lower. However, from the inclinations of the chromospheric and the photospheric field lines we would expect the fast downflowing component to lie higher (see Fig. 9b: the red and green arrows fit better together). In this case a shock would have to lie between the components.

Can we distinguish between the uncombed model and the cloud model? A non-linear force-free magnetic field extrapolation applied to this region nicely reproduces the overall topology of the chromospheric magnetic field (Wiegelmann et al. 2005). The agreement between the extrapolated magnetic loops and the magnetic field structure as inferred from the dominant He I component (i.e. the component with the larger filling factor) is remarkable. Since the boundary condition of the extrapolation has only a single magnetic component, the extrapolations fail to reproduce the two-component structure at the footpoints of the loops. Therefore the extrapolations cannot help to distinguish

between the uncombed and the cloud model. However, the inclination angles retrieved from the extrapolations follow within the error bars the inclination of the dominant component. It is interesting to note that the small-scale fine-structure of the magnetic field in the layer of the He I line formation does not seem to be relevant for the large-scale loop structure of this active region.

According to the argument of Schmidt et al. (2000), the downflowing material would disturb or even destroy the unshifted atmospheric component. Our analysis shows that both atmospheric components have different magnetic field vectors. The resulting uncombed structure of the chromosphere allows for the coexistence of a flux tube containing gas at low velocities next to a flux tube carrying gas at large velocities without being disturbed, since the flux tube gas is confined to its respective flux tube. Even if both components lie above each other, the shock separating them should allow distinct velocities to be maintained.

5. Summary

Using spectropolarimetric data from the He I triplet we were able to obtain a time sequence of velocity maps at the footpoint of a magnetic arcade. In addition, we were simultaneously able to retrieve the full magnetic vector of the fast downflowing material and material at rest. We interpret the downflows as a consequence of the emergence of magnetic flux in the center of the observed region. This flux emergence transports photospheric material up to higher layers from where it falls down along the magnetic field lines to both loop footpoints. The speed of this asymmetric downflow of draining material reaches $\approx$15 km s^{-1} along one leg, and up to 40 km s^{-1} along the other. We interpret these high velocities as the consequence of the difference in gas pressure between the cool, highly magnetized region above the pore and the surrounding plage region. The low gas pressure inhibits the deceleration of the downflowing material and lengthens the downflow path. Signatures of heating at the sonic point are observed in the form of He I emission. The magnetic field vectors obtained in the loop footpoints indicate the presence of small, unresolved magnetic flux tubes with slightly different inclination angles, confirming the interpretation of the highly filamentary structure of the downflows by Kjeldseth-Moe et al. (1988). The presence of such a highly filamentary, "uncombed" chromosphere has to be confirmed by analyzing downflow regions observed at various viewing angles, since the differently inclined fields may lie at different heights along the line-of-sight, an analysis of a large number of supersonic downflows is currently being performed (Aznar Cuadrado et al. 2005).

Acknowledgements. The authors would like to thank Manolo Collados for his help during the observing run. We are also grateful to Achim Gandorfer for helpful discussions and an anonymous referee for useful comments.

References

Andretta, V., & Jones, H. P. 1997, ApJ, 489, 375
Athay, R. G. 1965, ApJ, 142, 755
Avrett, E. H., Fontenla, J. M., & Loeser, R. 1994, in Infrared Solar Physics, ed. D. M. Rabin, (Dordrecht: Kluwer Academic Publishers), IAU Symp. 154, 35
Aznar Cuadrado, R., Solanki, S. K., & Lagg, A. 2005, in Chromospheric and Coronal Magnetic Fields, ed. D. E. Innes, A. Lagg, S. K. Solanki, & D. Danesy, (ESA Publication Division), ESA SP-596
Balasubramaniam, K. S. 2001, ApJ, 557, 366
Boris, J. P., & Mariska, J. T. 1982, ApJ, 258, L49
Brekke, P., Hassler, D. M., & Wilhelm, K. 1997, Sol. Phys., 175, 349
Brynildsen, N., Maltby, P., Fredvik, T., Kjeldseth-Moe, O., & Wilhelm, K. 2001a, Sol. Phys., 198, 89
Brynildsen, N., Maltby, P., Kjeldseth-Moe, O., & Wilhelm, K. 2001b, ApJ, 552, L77
Brynildsen, N., Maltby, P., Kjeldseth-Moe, O., & Wilhelm, K. 2004, ApJ, 612, 1193
Cargill, P. J., & Priest, E. R. 1980, Sol. Phys., 65, 251
Charbonneau, P. 1995, ApJS, 101, 309
Chou, D.-Y. 1993, in The Magnetic and Velocity Fields of Solar Active Regions, ed. H. Zirin, G. Ai, & H. Wang, IAU Colloq. 141: ASP Conf. Ser. 46, 471
Degenhardt, D. 1989, A&A, 222, 297
Degenhardt, D., Solanki, S. K., Montesinos, B., & Thomas, J. H. 1993, A&A, 279, L29
Dere, K. P. 1982, Sol. Phys., 77, 77
Evershed, J. 1909, MNRAS, 69, 454
Evershed, J. 1910, MNRAS, 70, 217
Frutiger, C. 2000, Ph.D. Thesis, ETH Zürich, Switzerland, Diss ETH, No. 13896
Frutiger, C., Solanki, S. K., Fligge, M., & Bruls, J. H. M. J. 2000, A&A, 358, 1109
Gebbie, K. B., Hill, F., November, L. J., et al. 1981, ApJ, 251, L115
Grossmann-Doerth, U., Schuessler, M., & Steiner, O. 1998, 337, 928
Kjeldseth-Moe, O., Brynildsen, N., Brekke, P., et al. 1988, ApJ, 334, 1066
Lagg, A., Woch, J., Krupp, N., & Solanki, S. K. 2004, A&A, 414, 1109
Müller, D. A. N., Peter, H., & Hansteen, V. H. 2004, A&A, 424, 289
Maltby, P. 1975, Sol. Phys., 43, 91
Maltby, P., Avrett, E. H., Carlsson, M., et al. 1986, ApJ, 306, 284
Mariska, J. T. 1988, ApJ, 334, 489
Martínez Pillet, V., Collados, M., Sánchez Almeida, J., et al. 1999, in High Resolution Solar Physics: Theory, Observations, and Techniques (ASP), ASP Conf. Ser., 183, 264
Martínez Pillet, V., Lites, B. W., Skumanich, A., & Degenhardt, D. 1994, ApJ, 425, L113
Mathew, S. K., Solanki, S. K., Lagg, A., et al. 2004, A&A, 422, 693
McClymont, A. N. 1989, ApJ, 347, L47
McClymont, A. N., & Craig, I. J. D. 1986, Nature, 324, 128
McClymont, A. N., & Craig, I. J. D. 1987, ApJ, 312, 402
Muglach, K., & Sütterlin, P. 1998, in Three-Dimensional Structure of Solar Active Regions, ed. C. E. Alissandrakis, & B. Schmieder, ASP Conf. Ser., 155, 341
Muglach, K., Schmidt, W., & Knoelker, M. 1997, Sol. Phys., 172, 103
Müller, D. A. N., De Groof, A., De Pontieu, B., & Hansteen, V. H. 2005, in Chromospheric and Coronal Magnetic Fields, ed. D. E. Innes, A. Lagg, S. K. Solanki, & D. Danesy (ESA Publication Division), ESA SP-596
Nadeau, D., & Maillard, J.-P. 1988, ApJ, 327, 321
Parker, E. N. 1978, ApJ, 221, 368
Penn, M. J., & Kuhn, J. R. 1995, ApJ, 441, L51
Peter, H., & Judge, P. G. 1999, ApJ, 522, 1148
Pneuman, G. W., & Kopp, R. A. 1978, Sol. Phys., 57, 49
Rachkowsky, D. N. 1967, Izv. Krym. Astrofiz. Obs., 37, 56
Rüedi, I., Solanki, S. K., & Rabin, D. 1992, A&A, 261, L21
Rüedi, I., Solanki, S. K., & Livingston, W. C. 1995, A&A, 293, 252
Sasso, C., Lagg, A., & Solanki, S. K. 2005, in Chromospheric and Coronal Magnetic Fields, ed. D. E. Innes, A. Lagg, S. K. Solanki, & D. Danesy (ESA Publication Division), ESA SP-596
Sasso, C., Lagg, A., & Solanki, S. K. 2006, A&A, 456, 367
Schmidt, W., Muglach, K., & Knölker, M. 2000, ApJ, 544, 567
Socas-Navarro, H., Trujillo Bueno, J., & Landi Degl'Innocenti, E. 2004, ApJ, 612, 1175
Socas-Navarro, H., Trujillo Bueno, J., & Landi Degl'Innocenti, E. 2005, ApJS, 160, 312
Solanki, S. K. 2003, The A&AR, 11, 153
Solanki, S. K., Lagg, A., Woch, J., Krupp, N., & Collados, M. 2003, Nature, 425, 692
Spadaro, D., Lanza, A. F., Lanzafame, A. C., et al. 2003, ApJ, 582, 486
Spadaro, D., Billotta, S., Contarino, L., Romano, P., & Zuccarello, F. 2004, A&A, 425, 309
Spruit, H. C. 1979, Sol. Phys., 61, 363
Teriaca, L., Banerjee, D., & Doyle, J. G. 1999, A&A, 349, 636
Teriaca, L., Falchi, A., Cauzzi, G., et al. 2003, ApJ, 588, 596
Thomas, J. H., & Montesinos, B. 1991, ApJ, 375, 404
Wiegelmann, T., Lagg, A., Solanki, S. K., Inhester, B., & Woch, J. 2005, A&A, 433, 701